ACCEPTED MANUSCRIPT
Review of Scientific Instruments
AIP Publishing
This is the author's peer reviewed, accepted manuscript. However, the online version of record will be different from this version once it has been copyedited and typeset.
PLEASE CITE THIS ARTICLE AS DOI: 10.1063/5.0338512

Cluster Assisted Soft-landing Hub (CLASH): An Instrument for Surface Desorption and Deposition Using a Pulsed Cluster Ion Source

B. Tomasetti,[1] J. Fréreux,[1] X. Urbain,[1] T. Schiltz,[1] A. Lorvelec,[1] C. Dupont-Gillain,[1] A. Delcorte,[1] and C. Lauzin[1]
Institute of Condensed Matter and Nanosciences, Université catholique de Louvain, 1348 Louvain-la-Neuve, Belgium

(*Electronic mail: clement.lauzin@uclouvain.be)

(Dated: 8 June 2026)

The soft desorption and landing of organic molecules using large cluster ions was demonstrated on ToF-SIMS analytical instruments equipped with a gas cluster ion source. A natural next step following this proof-of-concept is the development of a dedicated instrument for cluster assisted soft-landing. In this work, we present the design and conception of CLASH (Cluster Assisted Soft Landing Hub), an instrument equipped with a pulsed ion cluster source operated at 200 Hz to produce cluster ions. Distributions centered around Ar_{1650}^+ and $(CO_2)_{2100}^+$ were accelerated to 4.5 keV to sputter and deposit α-cyano-4-hydroxycinnamic acid (CHCA) from targeted samples onto collector surfaces. We detail, through experiments and SIMION (ion optics software) simulations, all components of the instrument and the challenges encountered in cluster formation, ionization, acceleration, and detection.

I. INTRODUCTION

Clusters are intermediate species between the gas and condensed phases. This represents an important place along a reaction coordinate leading to a phase transition or the formation of a solution. This unique position has attracted a lot of attention with the will to study clusters to better understand such reactions at the microscopic level.[1–4] In particular, the production of ionic clusters in combination with the use of ion optics lead to the possibility to probe species along this coordinate in a mass-selective manner. This capability with the use of molecular action spectroscopy, allows then to record the spectral signature of mass-selected species.[5] This has, for example, allowed to probe the phase transition of water from the gas to the solid phase, one molecule at the time. In this work, clusters of 475 ± 25 monomers were identified as the smallest entity for which, the spectral band of crystalline ice begins to dominate the infrared spectrum.[6] Advances in the study of ionic clusters have also provided clear evidence of their significance in our atmosphere[7] and across the solar system.[8]

Beyond the idea of joining the gas and the condensed phase in a step by step approach, clusters also have a large surface-to-volume ratio and a large number of constituents leading to a large density compared to the gas phase. These properties combined with the technology of intense and ultra fast laser led to the use of clusters of deuterated methane and molecular hydrogen in an attempt to enhance the efficiency of nuclear fusion.[9,10] The plasma produced by intense amplified femtosecond laser irridiation of atomic and molecular clusters can also be of interest to produce XUV[11] and X-ray radiation or multiply charged ions.[12]

These features also attracted considerable interest for producing cluster ion beam sources with tunable energy to be used as projectiles. In particular, they are used for high-precision surface processing techniques such as ion beam polishing. The latter has emerged as a critical method for achieving ultra-smooth surfaces, especially in optics[13,14] and semiconductor manufacturing[15], where nanoscale precision is essential.[16] A major breakthrough was the development of gas cluster ion beam (GCIB) sources, which are capable of producing large cluster ions. These sources have significantly advanced secondary ion mass spectrometry (SIMS) as an analytical technique by enabling gentle sputtering, which allows both high-quality surface analysis and precise depth profiling. Furthermore, these clusters have been successfully employed to sputter a wide range of organic molecules from one surface to another, either for analytical purposes—such as acidic matrices[17,18] or the molecular content of mouse brain tissue[19]—or for soft-landing and synthesis experiments involving peptides and proteins.[20–22] However, these soft-landing experiments were all performed using commercial cluster sources installed on analytical ToF-SIMS instruments, which severely limited the experimenter's freedom, particularly with respect to sample size and cluster composition. Moreover, recent studies have demonstrated that cluster composition plays a critical role in determining secondary ion yield.[23,24]

The goal of this work was to build an instrument, named CLASH (Cluster-Assisted Soft-Landing Hub), to create an independent platform for exploring sputtering with a homemade cluster source. The manuscript is structured as follows, Sec. II presents a general description of the instrument, detailing each component from the pulsed cluster source through acceleration, mass selection, detection, and impact on the sample. Sec. III describes the sample preparation and ToF-SIMS analyses used to characterize the samples after deposition. Sec. IV shows the results, starting with the formation and detection of Ar_n^+ and $(CO_2)_n^+$. These clusters are then mass-selected and used to deposit α-cyano-4-hydroxycinnamic acid (CHCA) from a targeted sample onto another surface, called the collector.

II. GENERAL DESCRIPTION

The CLASH instrument consists of two chambers, as illustrated in Fig. 1A. The first chamber is used to produce the clusters using a pulsed supersonic expansion. The sec-

ACCEPTED MANUSCRIPT
Review of Scientific Instruments
AIP Publishing
This is the author's peer reviewed, accepted manuscript. However, the online version of record will be different from this version once it has been copyedited and typeset.
PLEASE CITE THIS ARTICLE AS DOI: 10.1063/5.0338512

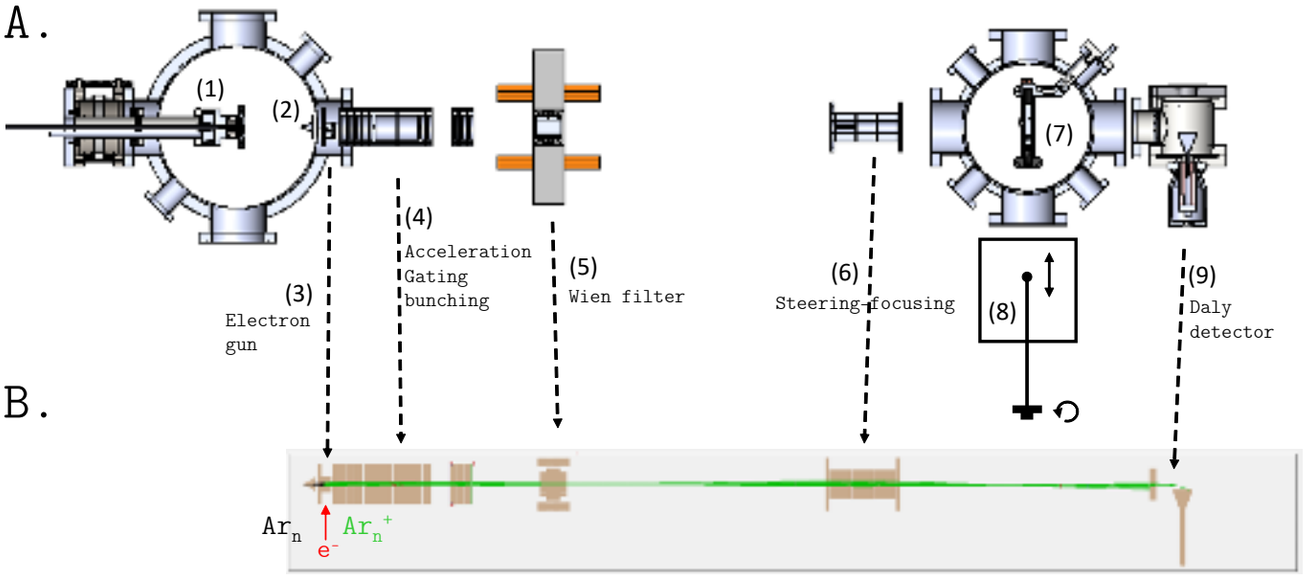


FIG. 1. (A) SolidWorks top view of the instrument: (1) pulsed valve, (2) skimmer, (3) electron gun, (4) acceleration, gating and bunching electrodes, (5) Wien filter, (6) steering and focusing electrode, (7) sample holder, (8) Load lock chamber featuring a translation system for sample insertion, (9) Daly detector. (B) SIMION simulation of CLASH. The parameter values of the simulation are provided in the supplementary material. Neutral Ar_{1000} clusters (FWHM = 125 atoms) are generated (in black), pass through the skimmer at 550 m.s^{-1}, and become ionized (in green) after crossing the electron beam (in red).

ond chamber, placed at a distance of 155 cm from the first, is devoted to the sample and soft landing. Both chambers are pumped by turbomolecular pumps with capacities of 2350 L/s and 2150 L/s for N_2 in the molecular flow regime ($P < 10^{-3}$ mbar), respectively. A home-built pulsed valve (1) is connected to a bellow (CF100/SEWB, Hositrad) that allows precise alignment and optimization of the circular nozzle position relative to the skimmer (2). The bellow has a travel distance of 26 mm. The pulsed valve is mounted on a CF40 tube and can be positioned in the center of the chamber for optical characterization of the jet, if it is found necessary. After passing through the skimmer, the clusters are ionized by an electron gun (3) and then accelerated, bunched, and referenced to the ground (4). All of the electrodes necessary for this process are housed within a T-shaped tube. A turbopump (260 L/s for N_2) is installed below. A Wien filter (5) is installed after acceleration. It is composed of two coils that create a magnetic field and electrodes that create an electric field perpendicular to the ion trajectory. A steering focusing lens (6) is placed in the drift tube and can be used to select the clusters in mass. Following a drift tube, the ions enter the sample chamber (7).

The sample chamber is connected to a load-lock chamber, which allows sample insertion without breaking the vacuum. This load-lock chamber is maintained by a separate turbomolecular pump and primary pump. A pneumatic valve separates the two compartments. This part was not drawn because the sample load-lock chamber and translation can were taken from an unused TRIFT™ ToF-SIMS instrument (Charles Evans & Associates, USA). Finally, ions can be detected using a Daly detector (9) placed after the sample chamber. A delay generator is used to synchronize all the timing signals, which are captured using an oscilloscope. Most of the CLASH elements were manufactured in-house at the UCLouvain mechanical workshop, and the corresponding drawings can be found in the supplementary material.

A. The pulsed supersonic expansion source

Previous soft-landing experiments with large clusters were performed using a commercial ToF-SIMS instrument equipped with a continuous supersonic expansion source.[20,22] Continuous beams offer advantages over pulsed operation, including simpler setup (only a nozzle is required) and improved stability of source conditions. In pulsed systems, the expansion temperature and cluster formation can vary during valve opening and closing, leading to fluctuations in cluster size distributions and internal energy, especially as valve timing changes with wear. These effects are generally more critical for clusters than for molecular beams. Therefore, some researchers in cluster science still prefer continuous expansions despite some of their disadvantages, *e.g.* the required higher pumping speed and the consequent smaller diameter of the nozzle affecting the cluster size (see Appendix).

However, pulsed supersonic expansions also offer important advantages. By restricting gas flow to brief pulses, pulsed valves reduce the overall background pressure in the vacuum chamber. In spectroscopy, this results in cleaner spectra and more precise measurements. For the purposes of this work, it also enables operation at higher backing pressures or with larger nozzle diameters, two parameters that increase the clus-

ACCEPTED MANUSCRIPT
Review of Scientific Instruments
AIP Publishing
This is the author's peer reviewed, accepted manuscript. However, the online version of record will be different from this version once it has been copyedited and typeset.
PLEASE CITE THIS ARTICLE AS DOI: 10.1063/5.0338512

ter formation. Moreover, the adaptability of the valve opening duration and backing pressure enables researchers to optimize conditions to generate clusters of specific sizes or composition. In addition, there is a growing demand for pulsed gas sources operating at frequencies between 1 and 5 kHz. This demand is driven by applications in atomic, molecular, and optical (AMO) physics, and nuclear fusion[9], where high peak density, low average pressure, and precise timing are critical. In particular, ultrafast laser systems frequently operate at repetition rates exceeding 1 kHz, requiring gas delivery systems capable of matching these high repetition rates while maintaining vacuum integrity and interaction efficiency.[25]

Several technologies are available for pulsing valves. **Solenoid valves** operate using a magnetic plunger inside a coil. For example, the Even-Lavie valve is capable of generating 20 μs pulses at repetition rates of up to 1 kHz and handling backing pressures as high as 180 bars.[26,27] **Lorentz force valves** rely on the force exerted on a pulsed current through a strip placed in a permanent magnetic field. Due to the large current (400–1000 A), the strip bends as a result of the Lorentz force. A pin attached to the center of the strip briefly opens the nozzle hole, typically 10-20 μs. However, they are limited to low repetition rates ($\approx$ 30 Hz) due to heating constraints.[28]

PZT actuators offer several advantages, including compactness, ease of mounting, low power requirements, and the ability to operate at high repetition rates well above 1 kHz. However, they generate relatively low forces ($\approx$ 0.5 N), making it difficult to open against high backing pressures. In addition, their performance is highly sensitive to the distance between the piezo element and the sealing surface, requiring frequent adjustments when heating the nozzle, changing backing pressures, or switching carrier gases. The Amsterdam piezovalve is capable of producing short pulses (7 µs) at a high repetition rate (5 kHz).[29] However, the valve does not allow real-time adjustment of the piezo-to-seal distance. Instead, this distance is set using three internal screws that fix the position when the valve body is opened. In 2018, Catanese *et al.* developed a design that preserves the advantages of piezo ceramics while enabling real-time external adjustments.[30] Their system achieved 11 µs pulses at repetition rates exceeding 5 kHz.

In this work, a very similar valve was developed. The description of the electrical circuit, mechanical drawings, and the assembly procedure can be found in the supplementary material (Sec.I). It also employs a PZT parallel bimorph actuator to pulse the beam, with the piezo-to-seal distance adjusted externally via a feedthrough mechanism that moves a piston. However, it differs from Catanese *et al.* in the fact that the O-ring is glued directly onto the PZT actuator, and the valve is fabricated in a CF40 format.

The design, dimension and ceramic kind of the piezomaterial have an impact on the deflection and resonance frequency that we can obtain. In the limit of a linear response and static operation, the deflection of a cantilever can be expressed as:[31]

$$\delta \propto d_{31} \frac{l^2}{t} \tag{1}$$

Where l is the free length of the cantilever. d_{31} is the charge piezoelectric constant (specified equal to -270 pm/V by the manufacturer) and t is the total thickness (0.5 mm).

The first natural resonant frequency, ν_1 of a clamped cantilever can be written:

$$\nu_1 \propto \frac{t}{l^2} \tag{2}$$

The piezo was cut to a length of 6.7 mm, and the free length, defined as the distance between the nozzle and the edge of the clamp, is l = 4.8 mm. Scaling these values, the expected deflection at 200 V is approximately 0.027 mm, and the resonant frequency is estimated at 71 kHz. This is significantly higher than the operating repetition rate, which ensures stable operation at the 200 Hz used here. This also means that in the next version, the free length could be increased.

The piezoelectric actuator is controlled by a delay generator, which sends TTL pulses (0 to 5 V) to a fast high-voltage transistor switch (HTS 61-01-GSM, BEHLKE). The details concerning the circuits driving the piezo are provided in the supplementary material. In particular, we had to pay particular attention to the current that one can deliver to such a device to perform at high repetition rate and over a short time.

The results presented here were obtained using a first version of the valve, for which leaks and the straight propagation of the pulsed gas were checked using a schlieren imaging setup (described in Ref.[32]). The next version could address several limitations by incorporating an oval piston, a differential screw for enhanced precision, and an adjustable piezo free length, whereas this parameter was fixed in the current version.

B. Ionization and acceleration

After passing through the skimmer, whose design is discussed in the supplementary material, the cluster must be ionized and accelerated. Fig. 2A presents a SIMION simulation of the ion optics mounted in CLASH, while Fig. 2B shows a photograph of the mechanical assembly prior to the latest modifications, including the addition of components (7) and (8) and ceramic beads around the cables. The starting point of this simulation is a beam of neutral particles (in black), whose mass follows a Gaussian distribution (mean = 40,000, FWHM = 5,000), generated with a speed of 550 m/s and a cone direction distribution with a half angle of 4°. This beam passes through a skimmer, then becomes ionized (in green) after crossing the electron beam (in red). It should be noted that ceramic pearls were placed around the cables due to the necessity to prevent discharges when the voltage applied increases.

The ion optics system is inspired by the STARGATE instrument.[5] From left to right, the neutral clusters (black) pass through a grounded plate that supports a custom-built electron gun (details in the supplementary material). Then, they move through a series of circular lenses. Lens 1 and Lens 2 guide the beam to the entrance of the buncher.

ACCEPTED MANUSCRIPT
Review of Scientific Instruments
AIP Publishing
This is the author's peer reviewed, accepted manuscript. However, the online version of record will be different from this version once it has been copyedited and typeset.
PLEASE CITE THIS ARTICLE AS DOI: 10.1063/5.0338512

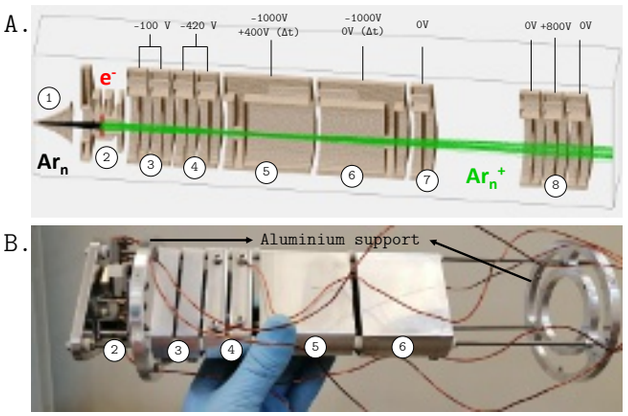


FIG. 2. (A) SIMION simulation of the electrode assembly used to ionize and accelerate the clusters. From left to right the beam crosses: (1) the skimmer, (2) the electron gun, (3) Lens 1, (4) Lens 2, (5) Gate 1, (6) Gate 2, (7) Lens 3, (8) einzel lens. (B) Picture of the assembly, for which elements (7) and (8), as well as the ceramic beads surrounding the cables, were added before installation.

In Fig. 2, the buncher, consisting of Gate 1 (5) and Gate 2 (6), compresses the beam spatially and references it to ground potential. At the exit of Gate 2, an electrode with a smaller aperture of 8 mm diameter is positioned (7). Finally, an einzel lens is placed at a certain distance from the buncher to further shape the beam.

The entire electrode assembly is supported by three threaded rods, with ceramic spacers that ensure proper separation. Two aluminum supports were machined with diameter of 99 mm, allowing them to fit inside a DN100 tube with three pressure screws. Mechanical drawings of the lens electrodes and the gates can be found in the supplementary material.

C. Wien filter

The Wien filter is a device consisting of orthogonal electric and magnetic fields that can be used as a velocity filter.[33] A particle moving inside the filter will follow a straight path and will be transmitted only if the magnetic force and the electric force are equal in magnitude in opposite directions. In that case, it can be shown that:

$$\frac{E}{B} = v \tag{3}$$

Which means that any combination of electric (E) and magnetic (B) fields will deflect all charged particles with velocity different than $v \pm \Delta v$. Fig. 3A shows the electrodes that were designed for the E field. Four rectangular electrodes (50 x 28 mm^2) were mounted to enable ion deflection in the $x-z$ and $y-z$ planes, where z is defined as the ion propagation axis. The mechanical drawing can be found in the supplementary material. Two copper foils with circular apertures (15 mm in diameter) were placed at the entrance and exit. The assembly was placed inside a DN63 tube. Around the tube, two coils were installed to generate a magnetic field by flowing a current through them. These coils are supported by an iron structure designed to guide the magnetic flux.

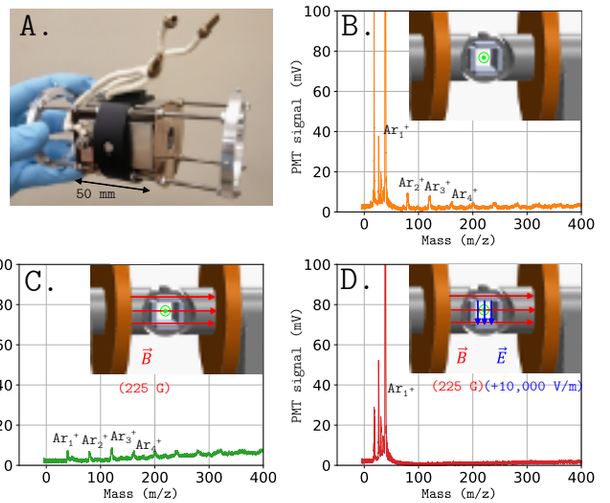


FIG. 3. (A) Picture of the rectangular electrodes of the Wien filter. (B) Mass spectrum when the Wien filter is off. The image in the top right corner shows the Wien filter with the beam passing in the center represented in green. (C) Mass spectrum when B = 225 G. (D) Mass spectrum when B = 225 G and E = 10,000 V/m. For each spectrum, the backing pressure was P_0 = 8 bar. The bunch was switched at 250 µs after the gas pulse for Gate 1 (-4000 V to +370 V) and Gate 2 (-4000 V to +0 V).

The coils and rectangular electrodes are shown in the upper right corner of the spectra in Fig. 3. The spectrum in the 0–400 m/z in Fig. 3B was recorded when the Wien filter was turned off. When a magnetic field of 225 G was established by flowing a current (5 A, 1.26 V) through the coils, small ions were deflected and not transmitted, resulting in a strong reduction of the Ar_1^+ signal (Fig. 3C). The intensity of larger clusters increased slightly, possibly due to a small correction in their trajectories.

Finally, when the electric field was also applied (Fig. 3D), the large clusters were no longer detected. In this configuration, the Wien filter acted as a velocity selector for Ar_1^+ and lighter ions (*e.g.*, residual species such as H_2O^+). These spectra were compared to SIMION simulations in the supplementary material.

In this work, the Wien filter is employed to filter out small ions and to correct the $x-y$ ion trajectories.

D. Ion steering and focusing

A steering and focusing einzel lens is placed just before the entrance of the sample chamber (see the supplementary material for technical drawings). While an einzel lens provides focusing, it also introduces spherical aberration. As a result, only about a quarter of the internal diameter of the central electrode should be used, as stated in Ref.[34]. Therefore, the lens must be significantly larger than the beam it is focusing.

ACCEPTED MANUSCRIPT
Review of Scientific Instruments
AIP Publishing
This is the author's peer reviewed, accepted manuscript. However, the online version of record will be different from this version once it has been copyedited and typeset.
PLEASE CITE THIS ARTICLE AS DOI: 10.1063/5.0338512

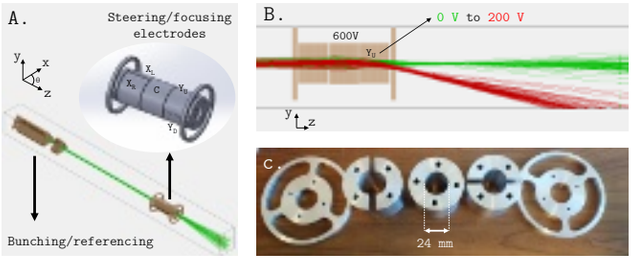


FIG. 4. (A) Focusing and steering lens placed at 1 m of the bunching/referencing unit in SIMION. (B) SIMION simulation of two identical beams. Red trajectories are obtained by applying 200 V on the upper half last electrode (Y_U). While green traces are obtained while maintaining grounding on the same electrode. (C) Picture of the electrodes.

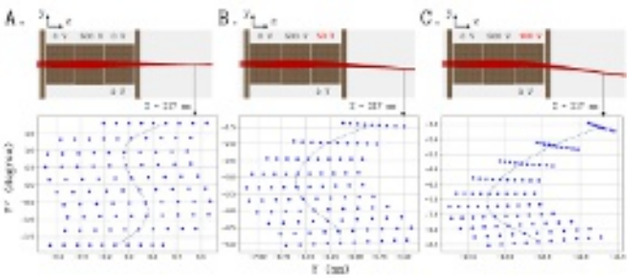


FIG. 5. The y–y' calculated emittance diagrams at the focus of the lens (217 mm) for different deflecting Y_U potentials: (A) 0 V, (B) 50 V and (C) 100 V. The dotted line shows the shape of the distortion.

The enlargement of the einzel lens reduces the available space for separate steering electrodes. Although space is not a significant issue for the CLASH instrument, it is beneficial to combine the steering and focusing functions into a single set of electrodes. In this design, the first and third electrodes, which are typically kept at the same potential, are split into half and separated. Each of the four half-electrodes can be independently activated with different potentials, allowing for steering in any direction.

Fig. 4A presents the SIMION simulation of the lens positioned 1 m after the skimmer. The beam consists of a distribution centered around $Ar_{1000}{}^{+}$ (FWHM = 125 atoms) and emerges from the bunching and referencing unit at 1 keV. The lens has five electrodes, each with an adjustable potential: X_R and X_L deflect the beam in the x-direction, C is the central electrode (which is not split in half), and Y_U and Y_D deflect the beam upward and downward, respectively. In Fig. 4B, the same beam is simulated, but represented in red when 200 V is applied to the Y_U electrode, affecting beam's trajectory. A strong focus is obtained by applying 600 V to the central electrode C. Fig. 4C shows a photograph of the manufactured aluminum electrode. The lens is supported by two grounded aluminum mounts, each with four holes and an outer diameter of 95 mm. These mounts were machined to hold the electrodes in place. Side pressure screws ensure proper centering and secure the assembly within a DN 100 tube. The electrodes are separated by ceramic spacers to maintain electrical insulation.

In order to evaluate the deflection aberration of this lens, a representative ion beam was used. $Ar_{1000}{}^{+}$ ions were accelerated to 1 keV. The ion array starts 50 mm upstream of the grounded support (at $z = 0$). The ions are initially spaced symmetrically about the center of the electrodes ($y = 0$), within a range of ± 5 mm along the y-axis, in steps of 1 mm. Their angular divergence (y') is also symmetrically distributed about $y' = 0$, within a range of $\pm 0.25°$, in steps of $0.05°$. This forms a square array of 100 ions in the y–y' phase space.

Beam focusing is achieved by raising the central electrode to 500 V. Fig. 5A shows the resulting y–y' emittance diagram when the beam is focused at 217 mm, with no net deflection at the focal point. The emittance plot exhibits an "S"-shaped distortion, as indicated by the dotted line.

There is no displacement or divergence in the x-direction. Due to the azimuthal symmetry of the lens, the x–x' emittance diagram would be identical.

In Fig. 5B, a positive 50 V bias is applied to the upper half of the exit electrode (Y_U). As a result, the beam is deflected downward. The y–y' emittance diagram at the focus now exhibits a "U"-shaped distortion. This deformation elongates the beam along one axis and is characteristic of sextupole aberration (see Refs.[35,36] for a mathematical description of the aberrations). Unlike the "S"-shaped distortion, the sextupole component introduces nonlinear distortions that generate asymmetries and tails in phase space, degrading beam quality without increasing the true emittance. In addition, this distortion is known to grow with increasing deflection.[36] This effect is further demonstrated in Fig. 5C, where the deflection voltage is increased from 50 V to 100 V, resulting in a more pronounced distortion of the emittance diagram.

To minimize beam distortion—particularly that caused by the sextupole component—an alternative electrode design should be considered in the future and adopted as the standard when both focusing and steering are required. This improved design involves introducing a diagonal slit in the central electrode, a concept studied by Mandal *et al.* for low-energy beams.[36]

E. Ion detection

Mass distribution measurement is a challenge well documented in the literature. This is due to dissociative ionization processes[37] and ion detection efficiency.[38–40] In particular, the efficiency of a microchannel plate (MCP) detector, which relies on secondary electron emission, decreases with increased mass and decreased impact energy. It has been shown that the efficiency for the detection of cationized polystyrene (PS; 10,000 amu) is approximately 80% at an impact energy of 20 keV and drops to 5% at 5 keV.[38]

For CLASH, an electrostatic Daly detector was built in which incoming ions are accelerated toward a conversion electrode, which is held at a high negative potential (typically around -15 kV).[41] When ions hit the electrode, they generate secondary electrons. The secondary electrons are accelerated

ACCEPTED MANUSCRIPT
Review of Scientific Instruments
AIP Publishing
This is the author's peer reviewed, accepted manuscript. However, the online version of record will be different from this version once it has been copyedited and typeset.
PLEASE CITE THIS ARTICLE AS DOI: 10.1063/5.0338512

away from the conversion electrode by a strong electric field and directed toward a scintillation crystal. Upon impact, these electrons excite the crystal, leading to the emission of photons. The emitted photons are then converted into electrons at the photocathode and subsequently amplified by the photomultiplier tube (PMT). A high voltage of +1 kV is applied to the PMT for all measurements in this work to ensure consistent comparison.

Fig. 6 presents the home-built Daly detector alongside its SolidWorks drawing. The conversion electrode is a coated aluminum electrode with a well-maintained surface, originally part of a magnetic Daly detector.[42] Due to the high potential applied to the electrode, a custom connection system was designed. The electrode is screwed into an insulating ceramic component with a conductive extremity. The ceramic is enclosed within a protective cap, where the connector is securely plugged and sealed.

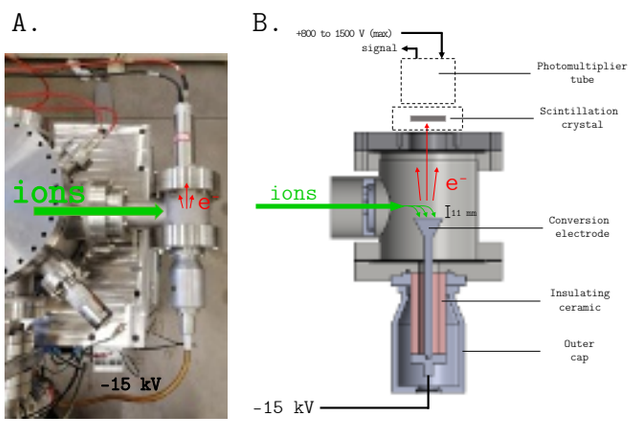


FIG. 6. (A) Picture of the home-built Daly detector fixed at the extremity of the sample chamber. (B) SolidWorks drawing of the detector.

In Sec. IV, this detector is employed to measure cluster distributions including a few thousand atoms. However, similar to an MCP, its detection principle relies on electron emission. Consequently, the measured distributions may not accurately reflect the true ones due to potential biases in detection efficiency. Nonetheless, the detector remains suitable for mass-selecting clusters within the ranges studied in this work. The experimenter should be aware of its reduced efficiency for higher masses, and post-acceleration to higher energies or other strategies should be implemented if larger clusters are to be measured.[43,44]

Finally, this design uses only an electric field, and the conversion electrode is not positioned directly in front of the beam. Therefore, if the beam energy exceeds 5 keV, the ions are not deflected sufficiently to hit the conversion electrode at -15 kV. For higher-energy beams, a design incorporating a magnetic field and a frontal conversion electrode was adapted from Ref.[41] and must be used in that case.

F. Sample holder and current measurement

A load-lock chamber is used to mechanically move a sample into the main chamber without breaking the vacuum. Fig. 7A shows a top view of the chamber when it is open. The cluster beam enters from the right and hits a sample holder plate positioned in front. The sample holder (top right of Fig. 7B) can slide along two rails, which are 3D-printed in PLA. Each rail contains a rectangular copper sheet that makes contact with the sample holder, the upper sheet is connected to an electrometer, and the one below is grounded.

The sample holder itself consists of two electrically insulated parts. It is designed to hold both solid samples (*e.g.*, screwed-in pieces) and copper foils, as illustrated in Fig. 7B. These foils are used for current measurements: the first foil is grounded and contains a central hole, while a second foil, positioned behind it, is used to measure the collected current.

This second foil is electrically connected to the upper part of the sample holder, which presses against the upper rectangular copper sheet, thereby establishing an electrical connection to an external BNC connector.

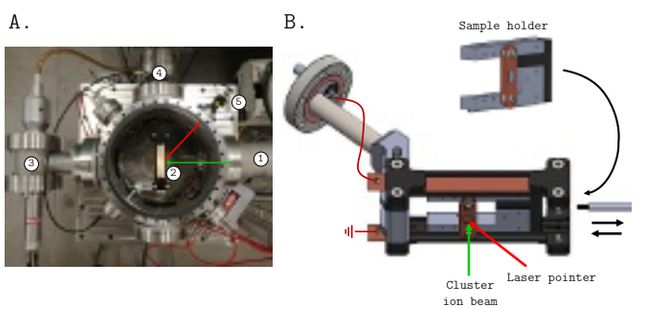


FIG. 7. (A) Top-view photograph of the sample chamber. The green arrow indicates the direction of the cluster ion beam. Components: (1) focusing and steering lens, (2) sample holder, (3) Daly detector, (4) load-lock chamber, and (5) laser pointer. (B) SolidWorks drawing of the sample holder (top right). This sample holder is screwed onto a translation can and positioned between two black PLA rails suspended inside the chamber. The top rail is connected to an external BNC connector, while the bottom rail is grounded.

With this design, a mass spectrum can first be measured using the Daly detector in order to mass-select a specific cluster size. The sample holder is then positioned so the ion beam strikes the copper foils, allowing ion current measurement and optimization with an electrometer or current-to-voltage amplifier. A laser pointer aids in aligning the system and optimizing the current at a fixed position. Finally, the sample holder is moved to place a mounted sample in the beam's path for deposition.

ACCEPTED MANUSCRIPT
Review of Scientific Instruments
AIP Publishing
This is the author's peer reviewed, accepted manuscript. However, the online version of record will be different from this version once it has been copyedited and typeset.
PLEASE CITE THIS ARTICLE AS DOI: 10.1063/5.0338512

III. MATERIAL AND METHODS

A. Sample preparation

For each deposition experiments, three Si wafers (15 x 15 mm^2, WAK2PN, Neyco, France) were cleaned for 15 minutes in a piranha solution (sulfuric acid/hydrogen peroxide, 4:1), rinsed with ethanol, and dried under a flow of N_2. One wafer was used as the target, onto which a thick CHCA layer was deposited by sublimation (2 h at 180 °C), resulting in a smooth layer 1.5 µm thick (R_a = 0.11 µm). The second wafer served as the collector for deposition, and the third as the cleaned Si reference.

B. ToF-SIMS analyses

ToF-SIMS analyses following the CLASH deposition experiments were performed using an IONTOF ToF-SIMS V commercial instrument. This instrument was used to quantify and image the molecular signal from the target and collector surfaces. A Bi_3^+ primary ion beam was used with a current of 0.4 pA and a cycle time of 100 µs. Large-area images were acquired by scanning the surface with a 500 µm × 500 µm raster, with two frames per patch and a pixel density of 256 × 256. Static analyses over 500 µm × 500 µm areas were also performed with an analysis time of 200 s. In this mode, the primary ion beam remains fixed and the signal is acquired from a single area without raster scanning. Three static analyses were carried out on each sample: one in the center and two located 1 mm from the edges, noting that both the collector and the target were 15 mm × 15 mm silicon wafers. Charge compensation was never used during the analyses.

IV. RESULTS AND DISCUSSION

A. Ar_n^+ Cluster formation and detection

Fig. 8A shows the superimposed mass spectra obtained for Ar_n^+ at 1 keV with a backing pressure P_0 = 6 bar. Mass-over-charge calibration is performed using the small clusters Ar_2^+ (34.8 µs), Ar_3^+ (42.6 µs), Ar_4^+ (49.38 µs), and Ar_{10}^+ (78 µs), for which the mass peaks are still resolved. The corresponding FWHM values are 0.35, 0.32, 0.32, and 0.52 µs, respectively. The intensity of these small clusters is enhanced by bunching them with a delay of 230 µs after the pulse. Ion bunching is achieved by switching the Gate 1 voltage from -1000 V to 70 V. The large cluster intensity is further optimized by bunching with a delay of 360 µs.

The steering and focusing electrode is used to mass-select the ions after a specific time-of-flight. A voltage of -150 V is applied to one of the half electrodes (X_L) to continuously deflect the beam, except during short pulses when the potential shifts to 0 V. In this experiment, short pulses of 20 µs were applied at increasing time-of-flight, allowing the selection of ions of increasing mass. Fig. 8A illustrates two key aspects.

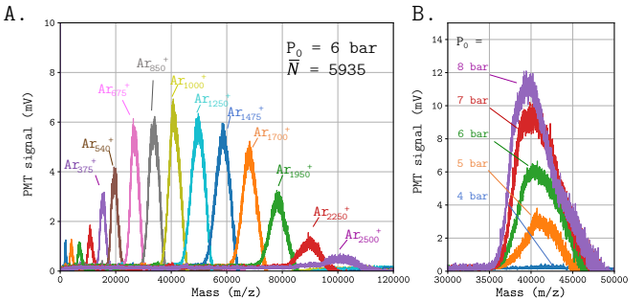


FIG. 8. (A) Distribution of Ar_n^+ cluster ions obtained by pulsing the steering electrode. Pulses of 20 µs were applied at increasing time delays, with each delay increasing by 50 µs steps. The backing pressure was fixed at 6 bar. (B) Cluster distribution centered around Ar_{1000}^+ obtained at different backing pressures. Voltages with the time delays referenced to t_0, the start of the gas pulse; Lens 1 (-950 V), Lens 2 (-360 V), Gate 1 (-1000 V to +70 V at t = 360 µs with Δt = 1.1 ms), Gate 2 (-1000 V to 0 V at t = 360 µs with Δt = 1.1 ms), X_L (pulsed at -150 V at variable t with Δt = 20 µs), X_R (0 V), C (-200 V), Y_U (0 V), Y_D (0 V).

First, it demonstrates the ability of CLASH to select mass distributions centered around a specific cluster size. A fixed $\Delta t = 20\,\mu s$ time gate corresponds to a larger absolute mass window for heavier clusters and amplifies energy/velocity spread effects (since $t \propto \sqrt{m}$), so large clusters appear broader even with the same temporal selection.

Second, the global mass distribution is also illustrated, with a sharp decline in intensity for small clusters and a broad distribution for larger clusters. When Ar_1^+ is mass-selected and bunched at a time delay of 230 µs, the maximum peak intensity reaches 1150 mV, with a full width FWHM of m/z 0.22 (data not shown). The intensity then decreases for small clusters and increases again, reaching a maximum near Ar_{1000}^+. This distribution shape was previously observed by Yamada[45] and can be explained by the fact that after a critical size N^*, cluster-cluster aggregation becomes the dominant growth mechanism, with minimal addition of individual monomers. This bimodal distribution is often observed in cluster beam experiments,[46,47] but detailed mechanisms of such growth cannot be extracted from mass spectra only. Nevertheless, this bimodal size distribution was also observed in soft ionization experiments, suggesting that it can be attributed to a transition in the cluster formation process.[48].

At this backing pressure, the heavier cluster distribution that was measured is centered around Ar_{2500}^+. With the installed nozzle (500 µm diameter, 15° half-cone angle), a backing pressure of 6 bar, and a stagnation temperature of 298 K, the semi-empirical Hagena law (see Appendix) predicts an average cluster size of 5935 Ar atoms. The experimentally measured distribution deviates significantly from this value; however, this deviation is expected. Electron-impact (EI) ionization induces extensive fragmentation of the clusters,[49,50] and an additional detection bias favoring lower masses further distorts the observed size distribution (see Sec. II E).

Fig. 8B shows the mass selection of Ar_{1000}^+ at different backing pressures. It can be seen that increasing the pressure

ACCEPTED MANUSCRIPT
Review of Scientific Instruments
AIP Publishing
This is the author's peer reviewed, accepted manuscript. However, the online version of record will be different from this version once it has been copyedited and typeset.
PLEASE CITE THIS ARTICLE AS DOI: 10.1063/5.0338512

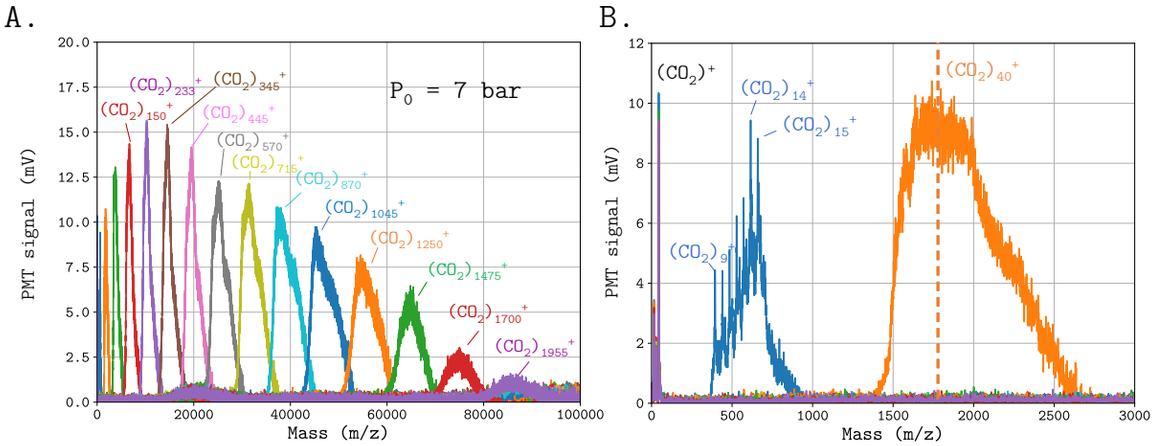


FIG. 9. (A) Distribution of $(CO_2)_n^+$ cluster ions obtained by pulsing the steering electrode. Pulses of 20 µs were applied at increasing time delays, with each delay increasing by 50 µs steps. The backing pressure was fixed at 7 bar. (B) Zoom-in view in the low mass range where cluster ion masses are still resolved.

increases the intensity. In this experiment, only the backing pressure was varied, while all other parameters were kept constant.

B. $(CO_2)_n^+$ Cluster formation and detection

CO_2 offers several potential advantages, as its clusters are nearly four times more stable than Ar clusters due to stronger van der Waals interactions. The binding energy of CO_2 clusters is 0.27 eV per atom, compared to 0.065 eV per atom for Ar clusters (average values obtained by molecular dynamic simulation in Ref.[51]). This increased stability facilitates the experimental production of larger clusters and reduces the likelihood of metastable decay as they travel down the ion beam column.

CO_2 cluster ion beams were generated simply by changing the feed gas. Fig. 9A shows the mass spectra obtained for $(CO_2)_n^+$. Mass calibration was performed using small clusters: $(CO_2)_2^+$ (36.8 µs), $(CO_2)_6^+$ (63.6 µs), $(CO_2)_9^+$ (77.8 µs), and $(CO_2)_{20}^+$ (116 µs), where the mass peaks remain well-resolved. Fig. 9B provides a zoomed-in view of a smaller mass range, highlighting the first two selected distributions. In blue, the first distribution shows that the different cluster ion peaks remain well-resolved and can be assigned. However, this is not the case for the next distribution, which is centered around $(CO_2)_{40}^+$.

The Hagena semi-empirical law (see Appendix) is not used here to determine the average CO_2 cluster size formed in the jet for two reasons. First, the law was primarily established and calibrated for rare gases, even though it provides a useful estimate for CO_2.[52] Second, experimental studies[53] show that, depending on the diagnostic technique, agreement on absolute or relative values is only achieved for $\Gamma < 10^4$, while in our case $\Gamma = 2.7\text{x}10^4$. Considering dissociative ionization, bias in detection for large masses, and the fact that the current experimental conditions fall outside the validated range, it is unsurprising that clusters smaller than those predicted by the Hagena formula are observed.

C. CHCA deposition

To perform the first CLASH deposition, a copper foil was used and bent to position the target and the collector so that the impact angle is at the optimal value for sputtering of 45°.[21] CHCA was chosen as a small molecule that is easily sputtered and has some interest for in situ matrix-enhanced secondary ion mass spectrometry.[17,18]

The experiment was performed sequentially. First, the sample holder was inserted and positioned so that the beam reached the Daly detector (position (1) in Fig. 10A). A spectrum of small clusters was initially measured for calibration and is shown in blue in Fig. 10B. A distribution centered around Ar_{1650}^+ (FWHM of 119 atoms) was then selected by time-of-flight. The beam energy was increased to 4.5 keV ($E/n = 2.73$ eV) to ensure soft sputtering.

After the size distribution measurement, the sample holder was moved toward the current measurement (position (2) in Fig. 10A). An average current of 0.4 nA was measured for Ar_{1650}^+ at a repetition rate of 200 Hz. Considering a pulse width of 20 µs with mass selection (X_L), this corresponds to a relatively high peak current of 100 nA, indicating that increasing the repetition rate could significantly enhance the current and, consequently the deposition rate. However, increasing the frequency of the pulsed valve resulted in higher beam current but did not improve the cluster intensity. In fact, at higher frequencies, the noise level at the Daly detector increased, and Ar^+ ions began to be detected. This is probably due to the higher pressure in the instrument. For this reason, the frequency was maintained at 200 Hz for this first deposition experiment.

The voltages were optimized to the following values, with the time delays referenced to t_0, the start of the gas pulse; Lens

ACCEPTED MANUSCRIPT
Review of Scientific Instruments
AIP Publishing
This is the author's peer reviewed, accepted manuscript. However, the online version of record will be different from this version once it has been copyedited and typeset.
PLEASE CITE THIS ARTICLE AS DOI: 10.1063/5.0338512

1 (-400 V), Lens 2 (-1800 V), einzel lens (+1000 V), Gate 1 (pulsed from -4000 V to +1000 V, at t = 330 µs with Δt = 1.1 ms), Gate 2 (pulsed from -4000 V to 0 V at t = 330 µs with Δt = 1.1 ms), X_L (pulsed from -250 V to 0V at t = 650 µs with Δt = 20 µs), X_R (0 V), C (-1000 V), Y_U (0 V), Y_D (0 V). The Wien filter was off during this deposition. The pressure in the jet chamber was around 3 x 10^{-4} mbar, and the pressure after the skimmer was around 4 x 10^{-5} mbar and decreased slightly over time.

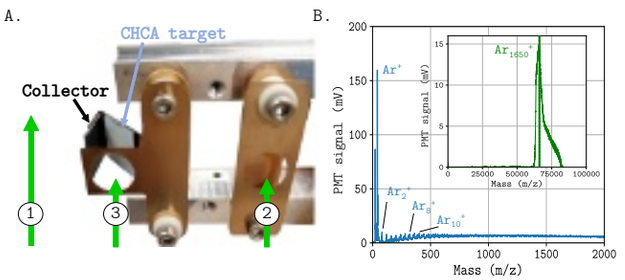


FIG. 10. (A) Picture of the sample holder with the different positions. (1) The ions (green arrow) follow a straight path toward the Daly detector (not shown), (2) optimization of the current and (3) target bombardment. (B) Mass spectra obtained with the Daly detector showing the lower mass cluster for calibration (blue) and the selection of a distribution centered around Ar_{1650}^+ (green).

After deposition using 2.89 x 10^{14} cluster ions with a distribution centered around Ar_{1650}^+ and an energy of 4.5 keV, 2D large-area ToF-SIMS analyses of the target, the collector and a cleaned Si wafer reference were performed (Fig. 11). The picture of the target and the corresponding $[CHCA+H]^+$ ToF-SIMS signal indicate that the center region was bombarded by the ion beam. The circular pattern observed arises from a circular aperture of 10 mm of diameter placed before the target and mounted on the sample holder (see Fig. 10A).

For the collector, a decrease in the Si signal relative to the reference, together with the detection of the CHCA molecular ion, confirms that CHCA molecules were deposited on its surface. This experiment highlights a key observation: the ion beam was not well focused and appeared to spread widely, consistent with the 10 mm diameter aperture placed in front of the target. The beam brightness can be further improved by introducing apertures and optimizing the lens system through adjustments to position, operating voltage, and design.

To demonstrate that other gases, such as CO_2, can also be used, a deposition experiment was performed using a cluster distribution centered around $(CO_2)_{2100}^+$ with a FWHM of 269 CO_2 molecules. At 200 Hz, the beam current was lower (0.1 nA) than for the deposition with Ar cluster ions (0.4 nA), and the applied dose was 7.33×10^{13} cluster ions. This time the Wien filter was on (5 A, 1.5 V), and a small electric field was applied to the electrodes of the Wien filter to optimize the current. Fig. 12A shows ToF-SIMS images of the CHCA target and the collector after deposition. Once again, the circular shape arises from the circular aperture placed in front of the target, indicating the poor focusing of the beam. Moreover, this aperture was connected to an electrometer, and a side current oscillating between 0.08 and 0.12 nA was detected.

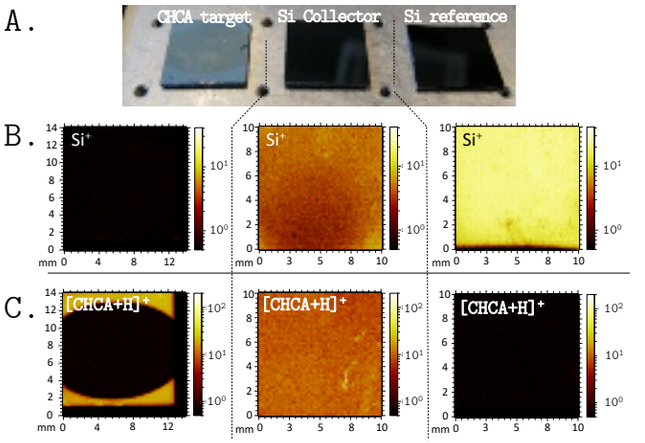


FIG. 11. (A) Picture of the different samples that were analyzed with ToF-SIMS after the deposition experiment. The CHCA target, the Si collector and a clean Si reference. (B) Si^+ and (C) $[CHCA+H]^+$ ion images for the different samples.

Fig. 12B shows the ion peak intensities measured on the collectors after the deposition experiments. The negative and positive ions of CHCA are compared to measurements performed on a Si reference wafer, which do not reflect actual CHCA signals but rather correspond to background interference and noise. The ion dose used for Ar_{1650}^+ deposition was 4.6 times higher than for $(CO_2)_{2100}^+$ deposition, so the plot was normalized to allow for a comparison. No significant differences were observed between the two CHCA deposition conditions. Future experiments will investigate other molecules and systematically assess the effects of ion energy and gas type on deposition rate and fragmentation.

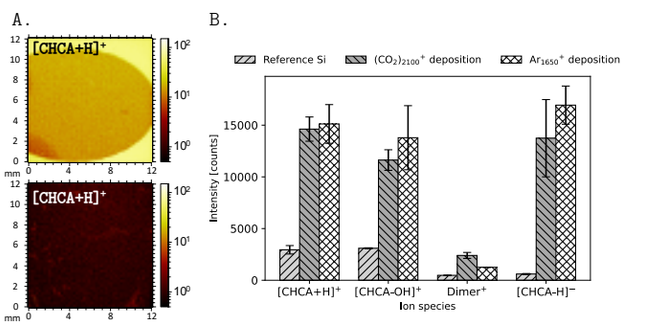


FIG. 12. (A) ToF-SIMS Bi_3^+ large images of the CHCA target and the collector after $(CO_2)_{2100}^+$ deposition. (B) Intensities of the CHCA ion species detected in positive and negative modes on the collector after deposition. $(CO_2)_{2100}^+$ deposition was performed with 7.33×10^{13} cluster ions, while Ar_{1650}^+ deposition used 2.89 x 10^{14} cluster ions. Thus, Ar_{1650}^+ deposition intensities were normalized by the dose ratio of 4.6.

ACCEPTED MANUSCRIPT
Review of Scientific Instruments
AIP Publishing
This is the author's peer reviewed, accepted manuscript. However, the online version of record will be different from this version once it has been copyedited and typeset.
PLEASE CITE THIS ARTICLE AS DOI: 10.1063/5.0338512

V. CONCLUSION AND FUTURE PROSPECTS

The construction of a new instrument for sputtering and soft-landing is presented and is based on the use of pulsed supersonic expansion to generate cluster ions. This was motivated by the goal of advancing the development of a state-of-the-art pulsed valve that offers greater adaptability. Indeed, at high operating frequencies, the beam approaches quasi-continuous behavior while allowing the use of larger nozzle diameters or pressure ratios, which favor the formation of large clusters. $Ar_n{}^+$ and $(CO_2)_n{}^+$ were mass-selected and used to deposit CHCA from a targeted sample onto another surface, called the collector.

This setup represents a first demonstration that it is feasible to build a soft-landing instrument using cluster ions generated by a pulsed source. However, further improvements are required to achieve a fully efficient system. The main limitation is found to be the focus of the beam. Implementing apertures and several current measurements along the beam path would provide a better understanding of the beam characteristics and enable subsequent adjustments, such as changes in lens positions, dimensions, or types (*e.g.*, upgrading to a diagonal-slit einzel lens). In addition, new versions of the valve could be developed, along with enhanced safety measures, such as an interlock between the primary and secondary pumping systems, allowing for longer or overnight deposition experiments. Finally, post-acceleration to higher energies is needed to detect heavier clusters.

SUPPLEMENTARY MATERIAL

Sec. I describes the pulsed valve in detail with a general description, the piezo electrical circuit, the valve assembly procedure, and technical drawings. Sec. II describes the skimmer from Beam Dynamics and compares its performance with a skimmer manufactured at UCLouvain. Sec. III describes the electron gun by providing the mechanical drawing of the assembly and the SIMION simulation. Sec. IV provides a description of the accelerating bunching electrodes. Sec. V describes the Wien filter with the assembly drawing and SIMION simulations. Sec. VI describes the steering and focusing lens. Sec. VII describes the sample holder assembly. Finally, Sec. VIII lists all the adjustable variables used for the SIMION simulation of the entire instrument and the values set for the simulation shown in Fig. 1.

ACKNOWLEDGMENTS

The authors acknowledge the financial support by the Fédération Wallonie Bruxelles, through the project "iBEAM" and "REACSURF" funded by its research program "Actions de Recherche Concertées" (Convention No. 18/23-090 and No. 24/29-139, respectively) and by the Fonds de la Recherche Scientifique - FNRS. A.D. is a Research Director of the FNRS. X.U. is a Senior Research Associate of the Fonds de la Recherche Scientifique - FNRS. C.L. thanks the FNRS financial support (CDR grant No. J.0113.23 and MIS grant No. F.4038.24).

DATA AVAILABILITY STATEMENT

The data that support the findings of this study are available within the article and its supplementary material. Simulations and 3D files are openly available in UCLouvain Dataverse at https://doi.org/10.14428/DVN/EWL3UZ.

Appendix: Hagena semi-empirical law

For experimentalists, it is essential to determine the cluster size as a function of nozzle geometry, gas type, and gas properties (temperature T_0 and backing pressure P_0). To address this, Hagena developed an empirical scaling law that quantifies how these parameters influence the kinetic conditions for cluster growth.[52,54] The average cluster size $\overline{N}$ can be described by the following semi-empirical scaling law for axisymmetric gas expansion through sonic and conical nozzles:[52,55]

$$\overline{N} = a\left(\frac{\Gamma}{1000}\right)^b \tag{A.1}$$

The Hagena parameter Γ is function of the backing pressure P_0 (mbar), the equivalent critical-section diameter d_{eq} (µm) of the nozzle and the gas temperature T (K):

$$\Gamma = K\frac{P_0 d_{eq}^{0.85}}{T^{2.28}} \tag{A.2}$$

K is the gas specific constant (1650 for Ar,[56] 3660 for CO_2,[57] and see Ref.[58] for other gases). The equivalent critical-section diameter d_{eq} was also introduced by Hagena and is equal to:

$$d_{eq} = \frac{0.74d}{tan\alpha} \tag{A.3}$$

α is the half opening angle of the conical nozzle. For a sonic nozzle $d_{eq} = d$.

The experimental information of $\overline{N}$ is often obtained using Rayleigh scattering.[59–62] Such studies try to better understand the cluster formation because deviation of the Hagena law are often observed. For instance, an effective equivalent sonic-nozzle diameter $d^*_{eq} = \delta d_{eq}$ was introduced to account for the deviation observed from the predictions.[60] These deviations from an ideal conical nozzle can be due to boundary layers effects that restrict the performance in cluster formation. The results of these experiments provide the value of the constants a and b to match the Hagena scaling law in the given interval of Γ parameter. In this work, when the cluster size is evaluated, the Γ parameter is calculated. Based on the interval

ACCEPTED MANUSCRIPT
Review of Scientific Instruments
AIP Publishing
This is the author's peer reviewed, accepted manuscript. However, the online version of record will be different from this version once it has been copyedited and typeset.
PLEASE CITE THIS ARTICLE AS DOI: 10.1063/5.0338512

Γ **range**	a	b	**Ref**
$350 < \Gamma < 1,800$	38.4	1.64	[63]
$1,000 < \Gamma < 7,300$	33	2.35	[52,55]
$2,100 < \Gamma < 14,000$	78	1.84	[52]
$10^4 < \Gamma < 10^6$	100	1.8	[53]

TABLE I. Experimentally determined values of a and b for different ranges of the Hagena parameter Γ.

summarized in Table I, the average cluster size $\overline{N}$ can be approximated.

[1]A. Mizoguchi, Y. Ohshima, and Y. Endo, "Microscopic hydration of the sodium chloride ion pair," Journal of the American Chemical Society **125**, 1716–1717 (2003).
[2]A. McKellar, Y. Xu, and W. Jäger, "Spectroscopic exploration of atomic scale superfluidity in doped helium nanoclusters," Physical review letters **97**, 183401 (2006).
[3]A. Barclay, A. McKellar, and N. Moazzen-Ahmadi, "Observing the completion of the first solvation shell of carbon dioxide in argon from rotationally resolved spectra," The Journal of Physical Chemistry Letters **13**, 6311–6315 (2022).
[4]F. Xie, D. S. Tikhonov, and M. Schnell, "Electric nuclear quadrupole coupling reveals dissociation of HCl with a few water molecules," Science **384**, 1435–1440 (2024).
[5]R. Bejjani, A. Roucou, X. Urbain, K. Moshkunov, G. Vanlancker, and C. Lauzin, "Stargate: A new instrument for high-resolution photodissociation spectroscopy of cold ionic species," Review of Scientific Instruments **92** (2021).
[6]C. C. Pradzynski, R. M. Forck, T. Zeuch, P. Slavíček, and U. Buck, "A fully size-resolved perspective on the crystallization of water clusters," Science **337**, 1529–1532 (2012).
[7]M. Farnik, "Bridging gaps between clusters in molecular-beam experiments and aerosol nanoclusters," The Journal of Physical Chemistry Letters **14**, 287–294 (2023).
[8]F. Postberg, S. Kempf, J. Schmidt, N. Brilliantov, A. Beinsen, B. Abel, U. Buck, and R. Srama, "Sodium salts in E-ring ice grains from an ocean below the surface of Enceladus," Nature **459**, 1098–1101 (2009).
[9]T. Ditmire, J. Zweiback, V. Yanovsky, T. Cowan, G. Hays, and K. Wharton, "Nuclear fusion from explosions of femtosecond laser-heated deuterium clusters," Nature **398**, 489–492 (1999).
[10]J. Sim, S. Lee, H.-i. Kim, Y. Noh, J. Song, C. Song, J. Won, and W. Bang, "Fusion yield enhancement via secondary beam-target reactions in laser-cluster experiments," Scientific Reports (2026).
[11]Y. Tao, R. Hagmeijer, H. M. Bastiaens, S. J. Goh, P. v. d. Slot, S. Biedron, S. Milton, and K. J. Boller, "Cluster size dependence of high-order harmonic generation," New journal of physics **19**, 083017 (2017).
[12]T. Ditmire, T. Donnelly, A. Rubenchik, R. Falcone, and M. Perry, "Interaction of intense laser pulses with atomic clusters," Physical Review A **53**, 3379 (1996).
[13]V. Collaboration, F. Beauville, D. Buskulic, R. Flaminio, F. Marion, A. Masserot, L. Massonnet, B. Mours, F. Moreau, J. Ramonet, *et al.*, "The VIRGO large mirrors: a challenge for low loss coatings," Classical and Quantum Gravity **21**, S935–S945 (2004).
[14]E. Bourelle, A. Suzuki, A. Sato, T. Seki, and J. Matsuo, "Sidewall polishing with a gas cluster ion beam for photonic device applications," Nuclear Instruments and Methods in Physics Research Section B: Beam Interactions with Materials and Atoms **241**, 622–625 (2005).
[15]K. Krishnaswami, S. R. Vangala, H. M. Dauplaise, L. P. Allen, G. Dallas, D. Bakken, D. F. Bliss, and W. D. Goodhue, "Molecular beam epitaxy on gas cluster ion beam-prepared GaSb substrates: Towards improved surfaces and interfaces," Journal of crystal growth **310**, 1619–1626 (2008).
[16]K. G. Xie, Y. Xie, and H. Deng, "Gas cluster ion beam smoothing technique: A review," Nanomanufacturing and Metrology **8**, 12 (2025).
[17]M. Lorenz, J. Zhang, A. G. Shard, J.-L. Vorng, P. D. Rakowska, and I. S. Gilmore, "Method for molecular layer deposition using gas cluster ion beam sputtering with example application *in situ* matrix-enhanced secondary ion mass spectrometry," Analytical Chemistry **93**, 3436–3444 (2021).
[18]K. Moshkunov, B. Tomasetti, T. Daphnis, V. Delmez, K. Vanvarenberg, V. Préat, M. Lorenz, J. Quanico, G. Baggerman, F. Lemiere, *et al.*, "Improvement of biomolecular analysis in thin films using *in situ* matrix enhanced secondary ion mass spectrometry," Analyst **146**, 6506–6519 (2021).
[19]B. Tomasetti, C. Lauzin, and A. Delcorte, "Enhancing ion signals and improving matrix selection in time-of-flight secondary ion mass spectrometry with microvolume expansion using large argon clusters," Analytical Chemistry **95**, 13620–13628 (2023).
[20]V. Delmez, H. Degand, C. Poleunis, K. Moshkunov, M. Chundak, C. Dupont-Gillain, and A. Delcorte, "Deposition of intact and active proteins *in vacuo* using large argon cluster ion beams," The Journal of Physical Chemistry Letters **12**, 952–957 (2021).
[21]V. Delmez, B. Tomasetti, T. Daphnis, C. Poleunis, C. Lauzin, C. Dupont-Gillain, and A. Delcorte, "Gas cluster ion beams as a versatile soft-landing tool for the controlled construction of thin (bio) films," ACS Applied Bio Materials **5**, 3180–3192 (2022).
[22]B. Tomasetti, M. Lakhdar, V. Delmez, C. Dupont-Gillain, C. Lauzin, and A. Delcorte, "Gas cluster ion beam-assisted deposition for fabricating dry multilayers containing enzyme and substrate with on-demand release," ACS Applied Materials & Interfaces **16**, 37248–37254 (2024).
[23]S. J. Lee, A. Hong, J. Cho, C. M. Choi, J. Y. Baek, J. Y. Eo, B. J. Cha, W. J. Byeon, J. Y. We, S. Hyun, *et al.*, "Characteristics of a mixed-gas cluster ion beam for time-of-flight secondary ion mass spectrometry," Applied Surface Science **572**, 151467 (2022).
[24]M. Lagator, B. Patel, S. Sheraz, and N. Lockyer, "Reactive gas cluster ion beams for enhanced drug analysis by secondary ion mass spectrometry," Analytical Chemistry **96**, 15185–15193 (2024).
[25]D. Irimia, R. Kortekaas, and M. H. Janssen, "*In situ* characterization of a cold and short pulsed molecular beam by femtosecond ion imaging," Physical Chemistry Chemical Physics **11**, 3958–3966 (2009).
[26]U. Even, J. Jortner, D. Noy, N. Lavie, and C. Cossart-Magos, "Cooling of large molecules below 1 K and He clusters formation," The Journal of Chemical Physics **112**, 8068–8071 (2000).
[27]U. Even, "The even-lavie valve as a source for high intensity supersonic beam," EPJ Techniques and Instrumentation **2**, 17 (2015).
[28]B. Yan, P. Claus, B. Van Oorschot, L. Gerritsen, A. Eppink, S. Van De Meerakker, and D. Parker, "A new high intensity and short-pulse molecular beam valve," Review of Scientific Instruments **84** (2013).
[29]D. Irimia, D. Dobrikov, R. Kortekaas, H. Voet, D. A. van den Ende, W. A. Groen, and M. H. Janssen, "A short pulse (7 μs FWHM) and high repetition rate (dc-5khz) cantilever piezovalve for pulsed atomic and molecular beams," Review of Scientific Instruments **80** (2009).
[30]A. Catanese, S. Horton, Y. Liu, and T. Weinacht, "Real-time adjustable, 11 μs FWHM,> 5 kHz, piezo electric pulsed atomic beam source," Review of Scientific Instruments **89** (2018).
[31]Q.-M. Wang, Q. Zhang, B. Xu, R. Liu, and L. E. Cross, "Nonlinear piezoelectric behavior of ceramic bending mode actuators under strong electric fields," Journal of Applied Physics **86**, 3352–3360 (1999).
[32]J. Fréreux, B. Tomasetti, A. Benidar, G. Liger-Belair, A. Himakar, M. Lakhan, R. Srikar, S. Nikhilesh, J. Gopalan, S. Rao, *et al.*, "The dynamics of champagne cork popping revisited through high-speed schlieren imaging and computational fluid dynamics simulations," Physics of Fluids **36** (2024).
[33]J. Bahng, J. Hong, M. C. Choi, M.-S. Won, and B.-S. Lee, "Development of wien filter for small ion gun of surface analysis," Review of Scientific Instruments **87** (2016).
[34]G. F. Rempfer, "Unipotential electrostatic lenses: Paraxial properties and aberrations of focal length and focal point," Journal of applied physics **57**, 2385–2401 (1985).
[35]P. Hawkes, "Lens aberrations," Focusing of charged particles **1**, 411 (1967).
[36]P. Mandal, G. Sikler, and M. Mukherjee, "An einzel lens with a diagonal-slit central electrode to combine steering and focusing of a low energy ion beam," arXiv preprint arXiv:1007.1592 (2010).
[37]M. Fárník and J. Lengyel, "Mass spectrometry of aerosol particle analogues in molecular beam experiments," Mass Spectrometry Reviews **37**, 630–651 (2018).
[38]I. Gilmore and M. Seah, "Ion detection efficiency in SIMS: Dependencies on energy, mass and composition for microchannel plates used in mass

ACCEPTED MANUSCRIPT
Review of Scientific Instruments
AIP Publishing
This is the author's peer reviewed, accepted manuscript. However, the online version of record will be different from this version once it has been copyedited and typeset.
PLEASE CITE THIS ARTICLE AS DOI: 10.1063/5.0338512

spectrometry," International Journal of Mass Spectrometry **202**, 217–229 (2000).
[39]R. Liu, Q. Li, and L. M. Smith, "Detection of large ions in time-of-flight mass spectrometry: effects of ion mass and acceleration voltage on microchannel plate detector response," Journal of the American Society for Mass Spectrometry **25**, 1374–1383 (2014).
[40]B. Schläppi, J. J. Ferreiro, J. H. Litman, and R. Signorell, "Sodiumsizer for neutral nanosized molecular aggregates: Quantitative correction of size-dependence," International Journal of Mass Spectrometry **372**, 13–21 (2014).
[41]N. Daly, "Scintillation type mass spectrometer ion detector," Review of Scientific Instruments **31**, 264–267 (1960).
[42]F. Brouillard and O. Godart, "Study of the focusing properties of a detector for slow ions," Nuclear Instruments and Methods **74**, 141–146 (1969).
[43]V.-T. Nguyen, K. Wien, I. Baranov, A. Novikov, and V. Obnorskii, "Detection of large cluster ions by ion-to-ion conversion," Rapid communications in mass spectrometry **10**, 1463–1470 (1996).
[44]S. Haugg, M. Creydt, R. Zierold, M. Fischer, and R. H. Blick, "Boostermicrochannel plate (BMCP) detector for signal amplification in MALDI-TOF mass spectrometry for ions beyond m/z 50000," Physical Chemistry Chemical Physics **25**, 7312–7322 (2023).
[45]I. Yamada, *Materials processing by cluster ion beams: history, technology, and applications* (CRC press, 2015) pp. 101–102.
[46]B. Schläppi, J. H. Litman, J. J. Ferreiro, D. Stapfer, and R. Signorell, "A pulsed uniform laval expansion coupled with single photon ionization and mass spectrometric detection for the study of large molecular aggregates," Physical Chemistry Chemical Physics **17**, 25761–25771 (2015).
[47]S. J. Lee, C. M. Choi, B. K. Min, J. Y. Baek, J. Y. Eo, and M. C. Choi, "Development of an argon gas cluster ion beam for ToF-SIMS analysis," Bulletin of the Korean Chemical Society **40**, 877–881 (2019).
[48]C. Bobbert, S. Schütte, C. Steinbach, and U. Buck, "Fragmentation and reliable size distributions of large ammonia and water clusters," The European Physical Journal D-Atomic, Molecular, Optical and Plasma Physics **19**, 183–192 (2002).
[49]P. Lohbrandt, R. Galonska, H. Kim, M. Schmidt, C. Lauenstein, and U. Buck, "Electron impact fragmentation of size selected Ar_n (n= 4 to 9) clusters," Atomic and molecular beams: the State of the Art 2000 , 623–636 (2001).
[50]J. Lengyel, A. Pysanenko, V. Poterya, J. Kočišek, and M. Fárník, "Extensive water cluster fragmentation after low energy electron ionization," Chemical Physics Letters **612**, 256–261 (2014).
[51]H. Tian, D. Maciążek, Z. Postawa, B. J. Garrison, and N. Winograd, "CO_2 cluster ion beam, an alternative projectile for secondary ion mass spectrometry," Journal of The American Society for Mass Spectrometry **27**, 1476–1482 (2016).
[52]O. Hagena and W. Obert, "Cluster formation in expanding supersonic jets: Effect of pressure, temperature, nozzle size, and test gas," The Journal of Chemical Physics **56**, 1793–1802 (1972).
[53]F. Dorchies, F. Blasco, T. Caillaud, J. Stevefelt, C. Stenz, A. Boldarev, and V. Gasilov, "Spatial distribution of cluster size and density in supersonic jets as targets for intense laser pulses," Physical review A **68**, 023201 (2003).
[54]O. F. Hagena, "Nucleation and growth of clusters in expanding nozzle flows," Surface Science **106**, 101–116 (1981).
[55]O. F. Hagena, "Cluster ion sources," Review of scientific instruments **63**, 2374–2379 (1992).
[56]J. Wörmer, V. Guzielski, J. Stapelfeldt, and T. Möller, "Fluorescence excitation spectroscopy of xenon clusters in the VUV," Chemical Physics Letters **159**, 321–326 (1989).
[57]J. M. Hollas and D. Phillips, *Jet spectroscopy and molecular dynamics* (Springer Science & Business Media, 1994).
[58]R. Smith, T. Ditmire, and J. Tisch, "Characterization of a cryogenically cooled high-pressure gas jet for laser/cluster interaction experiments," Review of scientific instruments **69**, 3798–3804 (1998).
[59]G. Chen, B. Kim, B. Ahn, and D. E. Kim, "Pressure dependence of argon cluster size for different nozzle geometries," Journal of Applied Physics **106** (2009).
[60]H. Lu, G. Ni, R. Li, and Z. Xu, "An experimental investigation on the performance of conical nozzles for argon cluster formation in supersonic jets," The Journal of chemical physics **132** (2010).
[61]Y. Tao, R. Hagmeijer, E. T. A. van der Weide, H. M. Bastiaens, and K.-J. Boller, "Revisiting argon cluster formation in a planar gas jet for high-intensity laser matter interaction," Journal of Applied Physics **119** (2016).
[62]B. R. Lee, P. K. Singh, Y. J. Rhee, and C. H. Nam, "Spatiotemporal characteristics of high-density gas jet and absolute determination of size and density of gas clusters," Scientific Reports **10**, 12973 (2020).
[63]U. Buck and R. Krohne, "Cluster size determination from diffractive he atom scattering," The Journal of chemical physics **105**, 5408–5415 (1996).